Enhanced light trapping in thin-films perovskite solar cells by photonic crystal structures

Cite as: AIP Advances 16, doi: 10.1063/5.0303011
Submitted: 18 September 2025 • Accepted: 30 December 2025 •
Published Online: 9 99 9999

View Online Export Citation CrossMark

Mounir Bouras,[1] Moufdi Hadjab,[1] Maroua Chahmi,[1] Salah Khennouf,[1] Abdelaziz Rabehi,[2] Takele Ferede Agajie,[3,a)] and Abdullah K. Alanazi[4]

AFFILIATIONS

[1] Department of Electronics, Faculty of Technology, University of M'Sila, University Pole, M'Sila 28000, Algeria
[2] Laboratory of Telecommunication and Smart Systems (LTSS), Faculty of Science and Technology, University of Djelfa, P.O. Box 3117, Djelfa 17000, Algeria
[3] Department of Electrical and Computer Engineering, Faculty of Technology, Debre Markos University, P.O. Box 269, Debre Markos, Ethiopia
[4] Department of Chemistry, Faculty of Science, Taif University, Taif, Saudi Arabia

[a)] **Author to whom correspondence should be addressed:** takele_ferede@dmu.edu.et

ABSTRACT

To boost light harvesting in perovskite thin-film solar cells, we introduce a dual photonic crystal (PhC) architecture that significantly enhances light trapping and device performance. A one-dimensional photonic crystal (1D-PhC), implemented as a distributed Bragg reflector composed of alternating dielectric layers, functions as a highly reflective and low-loss back mirror. Complementarily, a two-dimensional photonic crystal (2D-PhC) pattern is embedded in a flexible poly-dimethylsiloxane substrate replacing conventional glass, effectively minimizing front-surface reflection. The geometries of both photonic structures are carefully optimized to promote efficient photon diffraction and prolong the optical path within the absorber layer, thereby maximizing light absorption. This hybrid PhC configuration enables superior light trapping and enhances the optical field confinement in the active perovskite layer. In addition, interface engineering is employed to reduce carrier recombination losses, further boosting overall device performance. Numerical simulations, conducted using the rigorous coupled wave analysis method via SYNOPSYS RSoft CAD tools, demonstrate a notable improvement in the short-circuit current density (J_{sc}), which increases from 21.3 mA/cm^2 in the planar structure to 39.6 mA/cm^2, an enhancement of 85%. Correspondingly, the power conversion efficiency rises from 15.8% to 26.1%, representing a substantial 65% relative improvement. These results underscore the potential of photonic crystal integration for next-generation high-efficiency perovskite solar cells.

I. INTRODUCTION

Organometal halide perovskite solar cells have attracted considerable attention in recent years, achieving remarkable advancements in energy conversion efficiency.[1] Within just a few years, their power conversion efficiency (PCE) increased dramatically, rising from 3% in 2009[2] to over 22%, as reported by Yang *et al.*[3] Perovskites have emerged as a highly promising light-absorbing material for next-generation solar cells, owing to their key features such as strong absorption in the visible spectrum,[4] long carrier diffusion lengths,[5] high carrier mobility,[6] simple fabrication processes,[7] and low production costs.[6]

Perovskite solar cells (PSCs) are typically fabricated in two main architectures: planar and mesoporous. More recently, the integration of nanostructures with various dimensions and geometries into different solar cell designs has led to further improvements in efficiency. This approach not only reduces the amount of absorbing material required but also introduces more sophisticated cell architectures.[8,9] The incorporation of nanostructures makes the cells lighter, more flexible, and less bulky, while simultaneously enhancing their efficiency.

Nanostructures improve solar cell performance by enabling more effective light trapping within the absorbing medium,[10] facilitating carrier extraction,[11] and concentrating the electromagnetic

field in the active layer through different configurations. In light-trapping structures, modifying the direction of the light path within the active layer increases the interaction time between light and material, thereby improving optical absorption.[12,13] By scattering light into off-normal directions, the path length of photons within the active layer is extended, and the probability of reflection at each interface increases due to angular deviation. Consequently, light traverses the absorbing layer along multiple pathways, substantially enhancing the likelihood of absorption.[14] The efficiency of light-trapping mechanisms depends strongly on the wavelength of the incident light as well as the size and configuration of the nanostructures employed.[15]

The integration of light-trapping structures represents a key strategy for enhancing solar cell efficiency. Photons that are not absorbed during their initial pass can be reflected by a back reflector, thereby increasing their optical path length and enabling multiple passes through the device before eventual reabsorption. This process, commonly referred to as photon recycling,[16] significantly improves absorption efficiency. Traditionally, metallic layers such as aluminum (Al) and silver (Ag) have been employed as back reflectors in thin-film solar cell architectures. However, semiconductor–metal interfaces often introduce optical losses associated with surface plasmon resonance phenomena. Moreover, these metals typically exhibit limited diffraction capabilities and are prone to environmental degradation, such as corrosion.[17]

To maximize the efficiency of perovskite solar cells (PSCs), research efforts are focused on improving the core perovskite material and refining the overall device architecture. A key strategy is the inclusion of specialized transport layers [the electron transport layer (ETL) and the hole transport layer (HTL)], which are integrated to significantly reduce the rate of charge carrier recombination within the active absorption layer. These layers allow for the precise tuning of electron and hole mobilities (μ_e and μ_h, respectively) within the cell. Optimal device performance is achieved when these mobilities are balanced (i.e., $\mu_e/\mu_h \approx 1$), ensuring electrons and holes travel to their respective contacts at similar velocities. This balanced transport minimizes the time carriers spend co-located, thereby reducing recombination probability and leading to enhanced conversion efficiency.[18] This study specifically investigates the use of dual ETLs and dual HTLs to fine-tune this carrier mobility balance. The mobilities were characterized using the space-charge-limited current (SCLC) method on purpose-built electron-only and hole-only devices (with both single and dual layers), and the final perovskite solar cells were thoroughly evaluated under standard solar simulation (AM 1.5 G) to confirm the performance improvements achieved by advanced layer engineering.

In this work, we propose the incorporation of two-dimensional photonic crystals (2D PhCs) together with a Distributed Bragg Reflector (DBR) to enhance photon recycling and improve the efficiency of ultra-thin perovskite solar cells. The performance of these nanostructured thin-film perovskite solar cells is investigated through modeling and numerical simulations. The proposed design integrates 2D PhCs within the perovskite absorber layer, while the DBR serves as a wavelength-selective back reflector. This configuration enhances photon recycling, thereby strengthening light absorption within the perovskite thin film. Simulations are carried out using RSoft's DiffractMOD and Solar Cell Utility, which are based on the Rigorous Coupled-Wave Analysis (RCWA) algorithm. These tools are used to evaluate the optical behavior of the proposed architecture and to calculate the resulting power conversion efficiency (PCE).

II. PROPOSED PEROVSKITE SOLAR CELL DESIGN

Contact boundary conditions for perovskite solar cells involve ensuring a good energy level alignment at the interfaces between the perovskite layer and the charge transport layers (ETL/HTL) and electrodes. This is achieved by optimizing material selection, using surface treatments to passivate defects, and using buffer layers such as organic hole transport layers (HTLs) to suppress recombination and facilitate efficient charge extraction.

Planar Perovskite Solar Cells (PSCs) are widely utilized because their structure is relatively easy to manufacture, largely thanks to the solution processing techniques used to deposit the perovskite film. This architecture is defined by its simple, layered arrangement where the light-absorbing perovskite layer is centrally positioned, effectively sandwiched between two different charge-transporting layers (CTLs) and finally capped by the electrodes.[19] The specific organization of these CTLs determines the overall device configuration, which can be one of two main types: conventional (n–i–p) or inverted (p–i–n) architecture. The conventional n–i–p setup features the electron transport layer (n-type) closer to the transparent electrode, while the inverted p–i–n setup places the hole transport layer (p-type) adjacent to the transparent electrode. The choice between these architectures depends primarily on material compatibility and the desired device stability characteristics.[20]

To maximize the efficiency of perovskite solar cells, careful selection and structuring of the perovskite material are essential. Perovskites typically follow the chemical formula ABX_3, where A and B are organic and/or inorganic cations, and X is a halide anion. Figure 1 shows the crystal structure of the perovskite (PVK) material. Tuning the size of the A-site cation is crucial not only for maintaining charge neutrality in the lattice but also for adjusting the tolerance factor, which influences phase stability and structural distortions.[18,21] Adjusting the B–X bond length (and angles) is a key factor in determining the material's bandgap via changes in orbital overlap and lattice geometry.[22] Among the absorber materials most commonly used in perovskite solar cells are single-halide perovskites—such as $CH_3NH_3PbX_3$—which allow bandgap tuning by varying the halide (X = I, Br, Cl). Mixed-halide perovskites further broaden the possibilities: their photovoltaic performance and stability depend sensitively on the halide ratio because altering the composition modifies structural symmetry, lattice constants, the B–X–B bond angles, and the optical absorption edge.[23,24]

The efficiency of Perovskite Solar Cells (PSCs) is heavily dependent on the choice of the Hole Transport Material (HTL), which

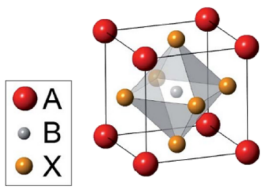

FIG. 1. The ABX_3 perovskite crystal structure.

must meet stringent criteria for optimal performance. An ideal HTL should exhibit high intrinsic hole mobility (μ_h) for efficient charge extraction, possess energy levels that are well-matched with the perovskite absorber to minimize interfacial energy barriers, and demonstrate robust long-term stability against environmental factors such as moisture and oxygen, as well as excellent photochemical and thermal stability. Crucially, for fabrication, especially in the conventional (*n–i–p*) architecture, the material must be solution-processable.[20] Poly(3-hexylthiophene) (P3HT) is a prominent, low-cost organic HTL candidate favored for its good charge carrier mobility and optimal bandgap alignment with solar irradiation. However, a key limitation of pristine P3HT is its relatively low electrical conductivity, which frequently results in depressed device conversion efficiencies, necessitating numerous studies dedicated to its conductivity enhancement [e.g., through additives or by using complementary materials such as a ZnS Electron Transport Layer (ETL) to boost overall stability].[25] These devices in configuration demonstrated a higher PCE, less hysteresis, and longer charge carrier lifetime. The superior performance was attributed to the improvement in the P3HT absorbance and the charge carrier lifetime to reduce the defects and suppress non-radiative recombination on the perovskite surface.[26]

Figure 2 illustrates the proposed design of the perovskite solar cell. In this architecture, a 100-nm-thick two-dimensional photonic crystal (2D PhC), formed at a poly-dimethylsiloxane (PDMS)/air interface, replaces the conventional thick glass substrate. PDMS is employed as a transparent medium with negligible absorption in the visible and near-infrared ranges. Beyond its optical transparency, it improves the device's mechanical durability and reduces surface reflections owing to its favorable refractive index. Eliminating the bulky glass substrate further enhances the structural flexibility of the cell compared with traditional planar configurations.

When illuminated from the PDMS side, the structured interface generates an antireflective effect at the air/PDMS boundary, facilitating greater light penetration into the device and thus improving efficiency. The active layer is composed of organic–inorganic halide perovskites ($CH_3NH_3PbX_3$, where X = Cl, Br, or I) with a thickness of ~500 nm. At the rear side, a distributed Bragg reflector (DBR) is incorporated to reflect unabsorbed photons—particularly in the longer wavelength region—back into the perovskite layer. This design compensates for the high bandgap and limited thickness of the absorber, thereby improving light harvesting. Remarkably, the overall device thickness is maintained at only ~1.5 μm.

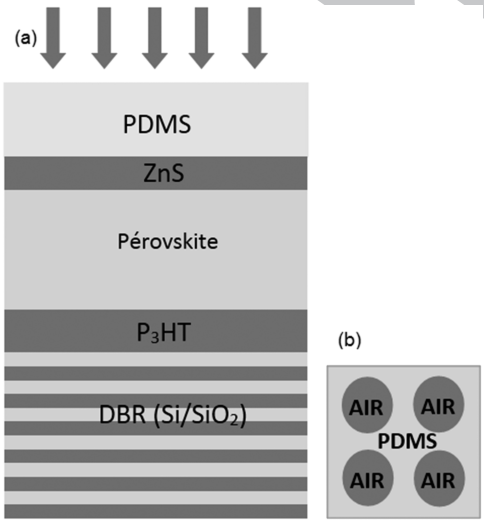

FIG. 2. (a) A schematic of the proposed structure of a perovskite on a DBR substrate. (b) Top view of 2D PhC grating layer with air cylinders.

The perovskite layer (region *i*) acts as the primary medium for exciton generation (bound electron–hole pairs) under illumination. The photogenerated charge carriers—electrons and holes—are subsequently extracted through the ETL and HTL, respectively. The efficiency of this collection process depends on the carriers' diffusion lengths as well as the electrical properties of the ETL and HTL. Exciton dissociation predominantly occurs at the ETL/perovskite and perovskite/HTL interfaces. Once separated, electrons are driven toward the ETL (n-type region), while holes migrate toward the HTL (p-type region). These processes of charge dissociation and transport are facilitated by the built-in electric field established across the ETL and HTL.[18–22]

III. METHODS

The performance of the proposed solar cell, including its power conversion efficiency (PCE), was evaluated using RSoft's DiffractMOD and LaserMOD, both of which are based on the Rigorous Coupled-Wave Analysis (RCWA) method. RCWA provides an efficient framework for solving Maxwell's equations in periodic media. In this semi-analytical approach, the longitudinal direction is treated analytically, while the transverse directions are solved numerically, enabling accurate calculations of reflection and transmission from periodic nanostructures. In RCWA simulations, the number of spatial field harmonics plays a critical role in determining accuracy. In Fourier space, both the refractive index profile and the electromagnetic fields are expanded as a function of the number of harmonics. Although increasing the harmonic order generally improves precision, it also significantly raises computational cost in terms of memory and runtime. To ensure an optimal trade-off between accuracy and efficiency, a convergence study was performed by running simulations with different harmonic orders. The results were found to converge and remain nearly stable when five or more harmonics were used. Consequently, a harmonic order of five was selected for all simulations in this study.[27]

RCWA uses the complex permittivity of the materials to model the full electromagnetic wave propagation and interaction with the structure. The complex refractive index ($n + ik$) is defined by the complex permittivity $\varepsilon = \varepsilon' + i\varepsilon''$, where ε' describes the refractive property and ε'' describes optical absorption and losses.[27]

LaserMOD is a photonic device simulation tool originally developed for analyzing the optical and electronic properties of semiconductor lasers through a self-consistent solution of electro-thermal transport and optical field propagation. In this study, LaserMOD was adapted for perovskite solar cell simulation by treating the active region as an absorbing medium rather than a gain medium. The optical intensity distribution, initially computed using the RCWA-based DiffractMOD module, was imported into LaserMOD to define the spatial generation profile within the device. The

software then recalculates the optical field at each bias point to determine the photogenerated current density under reverse electrical bias and applied optical excitation. This coupling enables a consistent evaluation of carrier transport, recombination, and potential distribution, providing realistic current–voltage (J–V), open-circuit voltage (V_{oc}), fill factor (FF), and power conversion efficiency (PCE) characteristics of the designed solar cell structure.[28,29]

LaserMOD includes a complete set of models for carrier mobility, radiative and non-radiative recombination, thermionic emission, quantum corrections, etc. The lifetimes for electrons and holes can be adjusted. The trap energy is a material parameter, which can be set with respect to the valence band edge. We use the default set here, which includes SRH and Auger recombination, carrier dependent losses (such as intervalence band scattering), bulk spontaneous recombination, and incomplete ionization.[29]

Physical modeling in LaserMOD is based on the MINILASE II code, which is described in more detail in Ref. 29. Results obtained using LaserMOD were published in Refs. 29 and 30. A general overview of the theory and concepts involved in the simulation of optoelectronic devices is given in Ref. 31.

The proposed device was modeled as a multilayer structure along the vertical (z) direction. The simulation algorithm applies lateral Bloch periodic boundary conditions and decomposes the solar cell into a series of thin layers (slices), for which reflection and transmission are computed individually. This layer-by-layer approach provides both physical insight into the optical response of the device and computational efficiency.[32]

The optical field distribution was computed using DiffractMOD, which solves the full vectorial Maxwell's equations via the RCWA algorithm under horizontally periodic boundary conditions. A square lattice (a = 0.38 μm) with Bloch boundaries was used, and the multilayer stack was discretized into 200 slices along z. The number of Fourier harmonics was varied from ±1 to ±9 using RSoft's MOST optimizer to ensure convergence. Integrated absorption and J_{sc} changed by <1% beyond ±5 harmonics, confirming convergence; hence, ±5 orders were used in all reported results (Fig. 3).

The total number of incident photons per unit area per unit time at a given solar spectrum S(λ) can be expressed as[33]

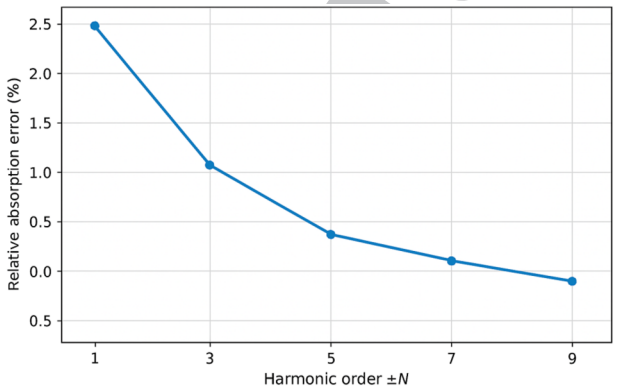

FIG. 3. RCWA convergence: absorption error vs Fourier harmonic.

$$N_s(\lambda) = \frac{S(\lambda)}{E_{photon}(\lambda)} = \frac{\lambda}{hc}\, S(\lambda). \tag{1}$$

The total number of incident photons per unit area per unit time at a given wavelength, $N_s(\lambda)$, also known as photon flux (photons m^{-2} s^{-1} nm^{-1}), can be calculated from the spectral irradiance of sunlight, S(λ) (W m^{-2} nm^{-1}), and the photon energy, $E_{photon}(\lambda) = hc/\lambda$, where h is Planck's constant, c is the speed of light, and λ is the wavelength.

The total absorption spectrum of the device, representing the cumulative absorption across all constituent layers, can be expressed as the sum of the absorption in each individual layer. Mathematically, this is given by

$$A(\lambda) = \sum_i A_i(\lambda). \tag{2}$$

The absorption spectra were calculated using RSoft's CAD tool. The number of photons absorbed within each layer can be determined as

$$N_i(\lambda) = \frac{S(\lambda)A_i(\lambda)}{E_{photon}(\lambda)} = \frac{\lambda S(\lambda)A_i(\lambda)}{hc}. \tag{3}$$

Poisson equations with interface and contact boundary conditions are usually expressed as follows:[34]

$$\frac{\partial}{\partial x}\left(\varepsilon_0\varepsilon_r \frac{\partial}{\partial x}\emptyset(x)\right) = q\left(p(x) - n(x) + N_D^+ - N_D^-\rho_{def}\right), \tag{4}$$

$$\frac{\partial}{\partial x}J_p(x) + G(x) - R(x) = \frac{\partial p}{\partial t}, \tag{5}$$

$$\frac{\partial}{\partial x}J_n(x) + G(x) - R(x) = \frac{\partial n}{\partial t}, \tag{6}$$

$$J_p = \frac{\mu_p}{q} p \frac{\partial E_{Fp}}{\partial x}, \tag{7}$$

$$J_n = -\frac{\mu_n}{q} n \frac{\partial E_{Fn}}{\partial x}. \tag{8}$$

The model couples Poisson's Eq. (4) with the continuity equations for electrons (6) and holes (5) to describe charge transport and electrostatic behavior in the semiconductor. Poisson's equation relates the electrostatic potential Φ(x) to the spatial distribution of charges, including electrons n, holes p, ionized donors N_D, acceptors N_A, and the defect charge density ρ_{def}. The continuity Eqs. (5) and (6) ensure charge conservation by describing how carrier concentrations evolve due to current divergence, generation (G), and recombination (R). The current densities for holes and electrons, given by Eqs. (7) and (8), depend on the gradients of the respective quasi-Fermi levels E_{Fp} and E_{Fn}, which govern carrier motion within the device. Carrier transport is further determined by their mobilities (μ_h and μ_e), while the dielectric constants (ε_0 and ε_r) define the material's electrostatic response. Together, Eqs. (4)–(8) provide a complete framework for modeling internal electric fields, charge dynamics, and the resulting operating voltage of the device.[35]

The general expression for the net recombination rate U is[36]

$$U = R - G_{thermal}, \tag{9}$$

where R is the total recombination rate and $G_{thermal}$ is the thermal generation rate, i.e., the rate at which carriers are generated even in the absence of light. In thermal equilibrium, $R = G_{thermal}$, which makes the net recombination rate $U = 0$. Under illumination in a solar cell, the total generation rate G_{total} becomes[36]

$$G_{total} = G_{light} + G_{thermal}, \tag{10}$$

where G_{light} is the photogeneration rate caused by absorbed photons. In solar cell operation, the most important contribution is the photogeneration rate G_{light} since it describes the creation of electron–hole pairs due to incident light.

The position-dependent photogeneration rate $G_{light}(x)$ is given by

$$G_{light}(x) = \int_{\lambda_{min}}^{\lambda_{min}} \alpha(\lambda, x).\Phi(\lambda, x).d\lambda, \tag{11}$$

where $\alpha(\lambda, x)$ is the absorption coefficient and $\Phi(\lambda, x)$ is the photon flux at a given wavelength λ and depth x. The limits λ_{min} and λ_{max} define the wavelength range of incident photons that contribute to photogeneration. This integral accounts for the spectral distribution of light and the material's ability to absorb it, making it a fundamental expression for modeling optical generation in solar cells.

In simple terms, G_{light} is proportional to the light intensity and to how strongly the material absorbs light at a given position in the device.

The total recombination rate R represents the sum of all physical processes through which an electron and a hole recombine and release energy. In most semiconductors, including perovskites, three dominant recombination mechanisms are typically considered: *Shockley–Read–Hall (SRH) trap-assisted recombination*, which occurs through defect states in the bandgap; *radiative recombination*, where an electron directly recombines with a hole and emits a photon; and *Auger recombination*, a three-particle process where the recombination energy is transferred to a third carrier instead of being emitted as light. Together, these mechanisms determine the overall recombination behavior and strongly influence the performance of solar cells,[36]

$$R_{total} = R_{SRH} + R_{rad} + R_{Auger}. \tag{12}$$

R_{SRH} is a non-radiative, trap-assisted recombination mechanism, where electrons and holes recombine via defect (trap) states within the bandgap. It is often the dominant loss mechanism in disordered materials, such as polycrystalline perovskites, significantly affecting carrier lifetime and device performance. R_{SRH} is commonly expressed as

$$R_{SRH} = \frac{np - n_i^2}{\tau_p(n + n_1) + \tau_n(p + p_1)}, \tag{13}$$

where n and p are the electron and hole concentrations, n_i is the intrinsic carrier concentration, and τ_n and τ_p are the lifetimes of electrons and holes associated with trap states, respectively. This expression captures how carriers recombine through defects in the bandgap, making *SRH* recombination a dominant loss mechanism in disordered materials such as polycrystalline perovskites, where it significantly affects carrier lifetime and device performance.

Radiative recombination R_{rad} is a band-to-band process in which an electron and a hole recombine directly, releasing the energy difference as a photon. This mechanism is the basis for light emission in LEDs and represents the theoretical minimum recombination loss in direct bandgap materials such as perovskites. The radiative recombination rate is given by

$$R_{rad} = B\left(np - n_i^2\right), \tag{14}$$

where B is the bimolecular recombination coefficient, and n, p, and n_i are the electron, hole, and intrinsic carrier concentrations, respectively.

Auger recombination R_{Auger} is a non-radiative, three-carrier process that becomes significant at very high carrier concentrations, such as under intense illumination or in highly doped regions. In this mechanism, the energy released by the recombination of an electron and a hole is transferred to a third carrier (electron or hole), which is excited deeper into its band instead of emitting a photon. The Auger recombination rate is expressed as

$$R_{Auger} = C_n n^2 p + C_p p^2 n, \tag{15}$$

where C_n and C_p are the Auger coefficients for electron-dominant and hole-dominant processes, respectively.

The short-circuit current density J_{sc} can be expressed as the integral over all wavelengths of the product of the external quantum efficiency (EQE) and the spectral photon flux density of the AM1.5G solar spectrum,[37]

$$J_{sc} = q \int EQE(\lambda)\Phi_{AM1.5G}(\lambda)d\lambda. \tag{16}$$

The short-circuit current density J_{sc} is calculated using the elementary charge $q = 1.602 \times 10^{-19}$, the external quantum efficiency $EQE(\lambda)$, which is the fraction of incident photons at wavelength λ that are converted into electrons, and the spectral photon flux density of the AM1.5G solar spectrum $\Phi_{AM1.5G(\lambda)}$ at the same wavelength λ.

Alternatively, for a simplified approximation, the integral can be scaled using the peak wavelength of the solar spectrum λ_{peak},

$$J_{sc} = \frac{q\lambda_{peak}}{hc} \int EQE(\lambda)\Phi_{AM1.5G}(\lambda)d\lambda, \tag{17}$$

where h is Planck's constant and c is the speed of light.

This formula essentially sums the contributions of all photons absorbed by the solar cell, weighted by the efficiency with which each photon generates current.

To obtain J_{sc} in mA/cm^2, divide the result by 1000 if the initial units are in A/m^2. The integral is taken over the wavelength range where the solar cell absorbs light.

The overall efficiency $\eta(\%)$ of the solar cell can be computed using the following expression:

$$\eta(\%) = \frac{P_{out}}{P_{in}} \times 100, \tag{18}$$

$$\eta(\%) = \frac{J_{sc} \times V_{oc} \times FF}{P_{in}} \times 100. \tag{19}$$

The performance of a solar cell can be described in terms of several key parameters. The output power (P_{out}) represents the electrical power delivered by the cell, while the incident power (P_{in}) corresponds to the incoming solar radiation. The short-circuit current density (J_{sc}) quantifies the current per unit area generated when the cell terminals are shorted, and the open-circuit voltage (V_{oc}) is the maximum voltage the cell can provide when no current flows. The fill factor (FF) indicates the ability of the solar cell to deliver maximum usable power, reflecting the combined effects of J_{sc} and V_{oc}. Together, these parameters determine the overall efficiency and performance of the solar cell.[35]

P_{out} corresponds to the electrical power that can be extracted from the solar cell, while the input power P_{in} is provided by the incident sunlight. The FF is a critical parameter that reflects how effectively the device converts the theoretical maximum power into practical output. In this context, η quantifies the overall capability of the solar cell to convert solar energy into electrical power.

IV. RESULTS AND DISCUSSION

Recent advances in hole-transport materials (HTMs) have focused on two main strategies to enhance device performance: (i) dopant engineering and dopant-free HTM design to improve conductivity and stability and (ii) interfacial defect passivation using self-assembled monolayers or small π-conjugated molecules to suppress non-radiative recombination. Controlled dopant optimization in spiro-OMeTAD and the development of dopant-free carbazole or phenothiazine derivatives have improved hole mobility while minimizing degradation. In parallel, interfacial passivation layers effectively enhance charge extraction and reduce trap-assisted losses, leading to higher V_{oc}, fill factor, and long-term stability. These chemical and interfacial strategies complement our optical optimization, ensuring that the enhanced photon absorption achieved through photonic crystal design translates into improved experimental PCEs.[22,23]

In this study, the reflection, transmission, and absorption coefficients were calculated using the RSoft CAD simulation tool. The real and imaginary parts of the refractive indices for each electron transport material (ETM) and hole transport material (HTM) were obtained from the literature. In our proposed design, the structure was optimized to determine the most suitable thicknesses of the alternating layers in order to effectively reflect the target wavelength range. Each layer of the solar cell was systematically tuned to maximize light-trapping and enhance optical performance.

As summarized in Table I, we analyzed the evolution of both the real and imaginary parts of the refractive index of each material as a function of the incident wavelength using the plasma-based optical model previously described. The specific optical parameters used for this calculation were assigned to each material according to the values listed in Table I.

This table summarizes the optical constants of the major materials used within the solar cell structure, specifically the real part of the refractive index (n) and the imaginary part (k) across the visible (Vis) and near-infrared (NIR) spectral regions. These parameters dictate how each layer interacts with incident light by defining its refraction, absorption, and transparency. Silicon exhibits a high refractive index in the visible range, combined with strong absorption (large k) at short wavelengths, which decreases sharply beyond its bandgap in the NIR region. In contrast, materials such as fused silica, ZnS, and PDMS feature low absorption ($k \approx 0$) across the visible and NIR regions, confirming their roles as transparent or weakly absorbing layers. P3HT, an organic semiconductor, displays a moderate refractive index with a distinct absorption peak in the visible spectral region, consistent with its π–π^* electronic transitions. The perovskite absorber ($CH_3NH_3PbX_3$) shows both a high refractive index and a high extinction coefficient in the visible spectrum, characteristic of its strong light-harvesting capability and high optical density.

The simulation utilized a comprehensive list of device parameters (detailed in Table II) to accurately model and fit the experimental data from the perovskite solar cells (PSCs). The only values adjusted to achieve this fit were the carrier mobility (μ_e and μ_h) within the perovskite layer, the trap density (N_t), and the charge capture coefficients (C_n and C_p). The extracted carrier mobilities were consistent with established values for $CH_3NH_3PbI_3$ PSCs. Carrier losses were modeled through bimolecular recombination in the bulk perovskite (using a coefficient of 1×10^{-9} cm^3 s^{-1}) and trap-assisted recombination (SRH) occurring at material interfaces (HTL/perovskite and perovskite/ETL) and grain boundaries (GBs). Crucially, the fitted coefficients revealed an asymmetry where the hole capture probability (C_p) is lower than the electron capture probability (C_n) ($C_p < C_n$). This asymmetry aligns with the experimental observation of long-lived holes in PSCs, indicating that holes are less prone to being trapped and lost at defect sites than electrons.

A. Application of 2D PhCs' antireflective coating

2D PhC structures have been proposed as an effective strategy to control light propagation in thin-film solar cells. In recent years,

TABLE I. Summary of dispersion $n(\lambda)$ and $k(\lambda)$.[38]

Material	n (Vis/NIR)	k (Vis/NIR)
Silicon (Si)	3.5–6.0	High in VIS/UV; ~0 in NIR (>1.1 μm)
Fused silica (SiO_2)	1.45–1.50	Extremely low (~0)
Zinc sulfide (ZnS)	2.2–2.5	Low (~0)
Polydimethylsiloxane (PDMS)	1.40–1.43	Low (~0)
Poly(3hexylthiophene) (P3HT)	1.5–2.0	High around absorption peak (0.5–0.65 μm)
Perovskite ($CH_3NH_3PbX_3$)	2.3–2.8	High in the visible region

TABLE II. Electronic parameters of the materials used in the solar cell.[24–28]

Parameters	SnO_2	PCBM	$MAPbI_3$	Spiro-OMETAD
Bandgap (eV)	3.6	2.1	1.55	3
Electron affinity (eV)	4.5	3.9	3.8	2.45
Dielectric permittivity (relative)	9.0	3.9	6.5	3
CB effective density of states (cm^{-3})	2.2×10^{18}	2.2×10^{19}	10^{19}	2×10^{18}
VB effective density of states (cm^{-3})	1.8×10^{19}	2.2×10^{19}	10^{17}	2×10^{19}
Electron mobility (cm^2/Vs)	100	10^{-3}	1	2×10^{-3}
Hole mobility (cm^2/Vs)	25	2×10^{-3}	1	2×10^{-3}
Electron lifetime (s)	10^{-7}	10^{-7}	10^{-6}	10^{-7}
Hole lifetime (s)	10^{-7}	10^{-7}	10^{-6}	10^{-7}
Uniform donor density N_D (cm^{-3})	5.635×10^{17}	5.635×10^{19}	10^{13}	0
Uniform acceptor density N_A (cm^{-3})	0	0	0	10^{17}

PhCs have gained significant attention as a promising approach to enhance light absorption in ultra-thin photovoltaic devices.[33,39–41] A photonic crystal is characterized by a periodic modulation of the refractive index, with the lattice constant comparable to the wavelength of incident light. This periodicity allows precise manipulation of light propagation and, in the case of ultra-thin perovskite solar cells, enables efficient light confinement within the absorber layer. using interference lithography and nanoimprint technology as effective techniques for patterning these 2D PhC structures directly onto the surface of thin membranes made from the promising new material polydimethylsiloxane (PDMS) for possible application in solar cells. Such membranes can be simply applied on different optoelectronic device surfaces and could modify the final optical properties.[42–44]

Figure 2(b) illustrates the schematic of an ultra-thin perovskite solar cell incorporating 2D PhCs, where a periodic array of holes is etched into the PDMS (polydimethylsiloxane) layer. Incident light couples into Bloch modes that propagate in-plane within the PDMS layer. When implemented on the front side of the solar cell, the 2D PhC reduces reflection and improves the coupling of incoming light into the active region. The cylinder radius of the photonic crystal is optimized to maximize diffraction, which occurs when the Fourier components of the dielectric function reach their highest values.

Simulations are performed across various configurations by simultaneously varying the lattice period (a) and the radius-to-period ratio (r/a) under normal light incidence. Initially, the cell is modeled with a fixed antireflective coating thickness close to a quarter-wavelength at the center of the optical spectrum. Specifically, the thickness is set to d_0 = 65 nm at the central wavelength λ_0 = 530 nm, corresponding to the peak of the solar emission spectrum.

For all simulations, a two-dimensional square lattice configuration is adopted as it can be practically fabricated over large areas using holographic lithography. Fabrication constraints also dictate the feasible ranges of geometric parameters: the lattice constant (a) is varied between 0.3 and 0.7 μm, while the radius-to-period ratio (r/a) is varied between 30% and 70%.

For this simulation, the optical index of PDMS is assumed to remain constant across all regions (*n*, *i*, and *p*). Under these conditions, the structure achieves a maximum integrated transmission of 93% and a minimum integrated reflectance of 5% at a = 0.38 μm and r/a = 62.5%. Notably, these results are in close agreement with previously reported optimal values for photonic crystals in solar cells, despite variations in the materials and geometric configurations considered in this work (Fig. 4).

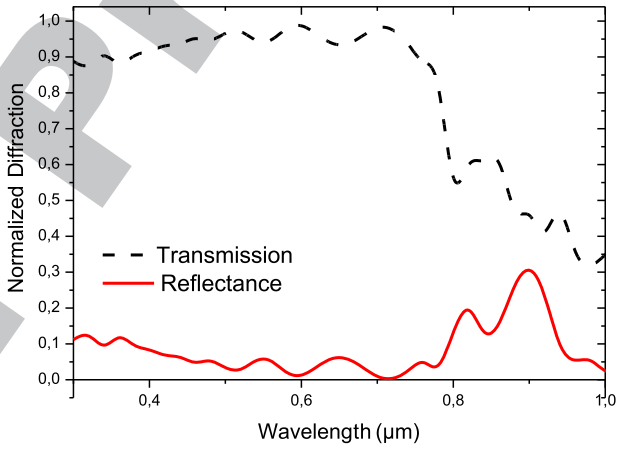

FIG. 4. Diffraction normalized from the PhC after optimizing the thickness of the layers.

As photons are effectively trapped within the proposed design, reflection of incident light is significantly reduced, as shown in Fig. 4. The trapped photons enhance the electric field distribution within the solar cell, leading to stronger light–matter interaction. It is observed that up to 90% of the incident photons can be confined within the extended effective thickness of the absorber layer (300–800 nm). This confinement minimizes optical parasitic losses and reflection, thereby increasing the integrated absorption spectrum of the device.

B. Application of DBR as wavelength-selective reflectors

The motivation for this work stems from recent studies by Sergey and Sajeev John, who demonstrated that light trapping and

photon recycling can significantly enhance power conversion efficiency in ultra-thin perovskite solar cells.[2] Building on this idea, we investigate photonic crystal-enhanced solar cells, where the conventional metallic back reflector is replaced with a distributed Bragg reflector (DBR). The DBR consists of a one-dimensional dielectric superlattice formed by alternating layers of silicon (Si) and silicon dioxide (SiO_2), chosen for their availability, ease of fabrication, and favorable optical and electrical properties. The dielectric contrast between Si (n_1 = 3.6) and SiO_2 (n_2 = 1.52) is optimized to generate a photonic bandgap (PBG) in the desired wavelength range, arising from the periodic modulation of the refractive index.[45–48]

The DBR structure is modeled as a sequence of alternating layers $(AB)^N$, where layer A is Si and layer B is SiO_2. The thickness of layer B is determined using the quarter-wave condition, $n_2d_2 = \lambda_0/4$, with λ_0 = 530 nm corresponding to the peak of the solar emission spectrum. The thickness of layer A is then optimized using the Multi-variable Optimizer and Scanner Tool (MOST) available in SYNOPSYS RSoft CAD (Fig. 5).

To characterize the optical properties of the DBR, the gap map method is applied to calculate the photonic bandgap. Figure 5 shows the bandgaps as a function of Si layer thickness (d_{Si}). Several bandgap regions are identified, offering different options for tuning the DBR to the desired operational wavelength. Three representative bandgap regions, highlighted in Fig. 5, are selected for the subsequent analysis.

It is essential to investigate the optical response of the photonic crystal reflector across the visible spectrum as such structures are highly relevant for photovoltaic applications. In particular, the reflector must provide sufficiently high reflectance over a broad spectral range in order to maximize photon confinement within the absorber layer and reduce transmission losses. Figure 5 presents the reflectivity spectra of the proposed distributed Bragg reflector (DBR) under transverse electric (TE) polarization. The DBR is designed with alternating silicon (Si) and silicon dioxide (SiO_2) layers, where the thicknesses are set to d_1(Si) = 35 nm and d_2(SiO_2) = 90 nm. These thicknesses were chosen based on the quarter-wave condition and further optimized to ensure constructive interference at the target central wavelength (λ_0 = 530 nm). To maintain high reflectance

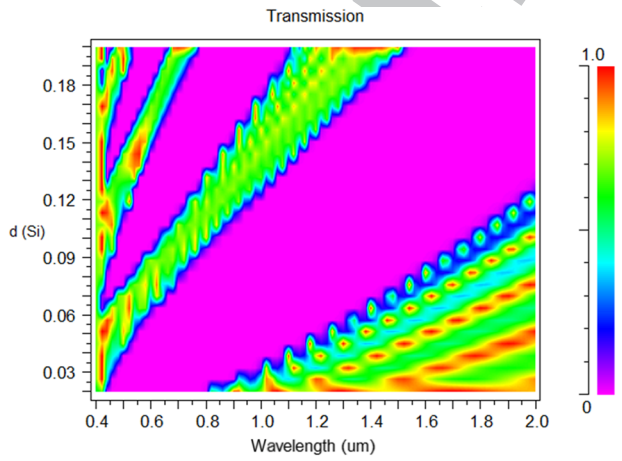

FIG. 5. Bandgap map of 1-D photonic crystal with Si/SiO_2 layers.

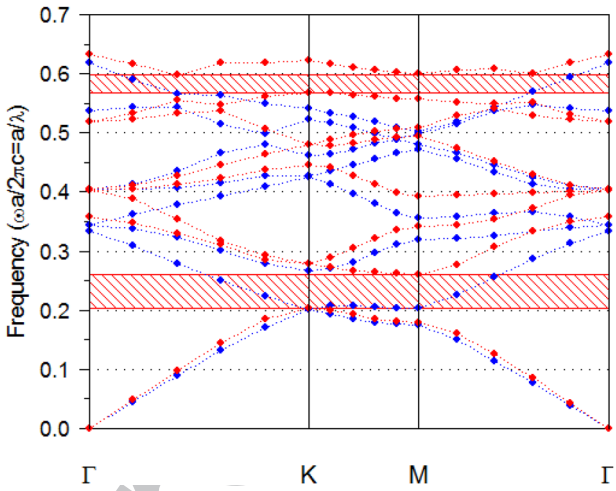

FIG. 6. Bandgap range achieved after optimization.

throughout the broader visible range (400–700 nm), these DBRs typically require 7–8 pairs of alternating (Si/SiO_2) layers.

The results indicate that the reflector exhibits strong photonic bandgap behavior, with peak reflectance exceeding around the designed central wavelength. The broad stop band generated by the periodic Si/SiO_2 structure ensures efficient reflection of incident photons, thereby enhancing light trapping within the solar cell. Such high reflectivity across the visible spectrum confirms the suitability of the DBR as a back-reflector in ultra-thin perovskite solar cells, where photon recycling and reduced parasitic absorption are critical for boosting overall device efficiency.

Figure 6 presents the reflectivity spectra of the binary photonic crystal (PhC) optical reflector for the transverse magnetic (TM) mode. In this study, the structure demonstrates an exceptionally broad photonic stop band of ~350 nm, achieving high reflectivity within the visible spectrum for both TE and TM polarizations and maintaining this performance across a wide range of incidence angles. This broad and polarization-independent high reflectivity highlights the potential of the proposed reflector for photovoltaic applications. The present work is focused on extending and further optimizing this wavelength range to maximize solar energy harvesting.

The distributed Bragg reflector (DBR) incorporated into the design diffracts light within the absorber layer and reflects it with minimal loss. Once inside the absorber, photons undergo multiple total internal reflections, resulting in strong light confinement. This process significantly increases the effective optical path length of the photons, enabling higher absorption even in ultra-thin absorber layers. Consequently, the DBR efficiently redirects the desired portion of the incident solar spectrum back into the active region of the solar cell.

This mechanism, commonly referred to as photon recycling, not only reduces optical losses but also enhances carrier generation by ensuring that unabsorbed photons have additional opportunities to interact with the absorber material. By improving the balance between transmission suppression and absorption enhancement, the

proposed DBR structure plays a crucial role in boosting the overall power conversion efficiency of the solar cell.

These reflective structures are generally deposited using thin-film techniques, with sputtering (particularly magnetron sputtering) and electron beam evaporation being the most common methods, offering high film quality. Chemical Vapor Deposition (CVD) can also be used, although it often requires higher temperatures. A significant advantage is the DBR's compatibility with flexible substrates, particularly when using low-temperature techniques such as sputtering. Achieving good mechanical stability and resistance to bending cycles in flexible devices relies on an optimal DBR design that balances layer number, maintains low film roughness to prevent light scattering losses, and ensures excellent adhesion to the substrate.

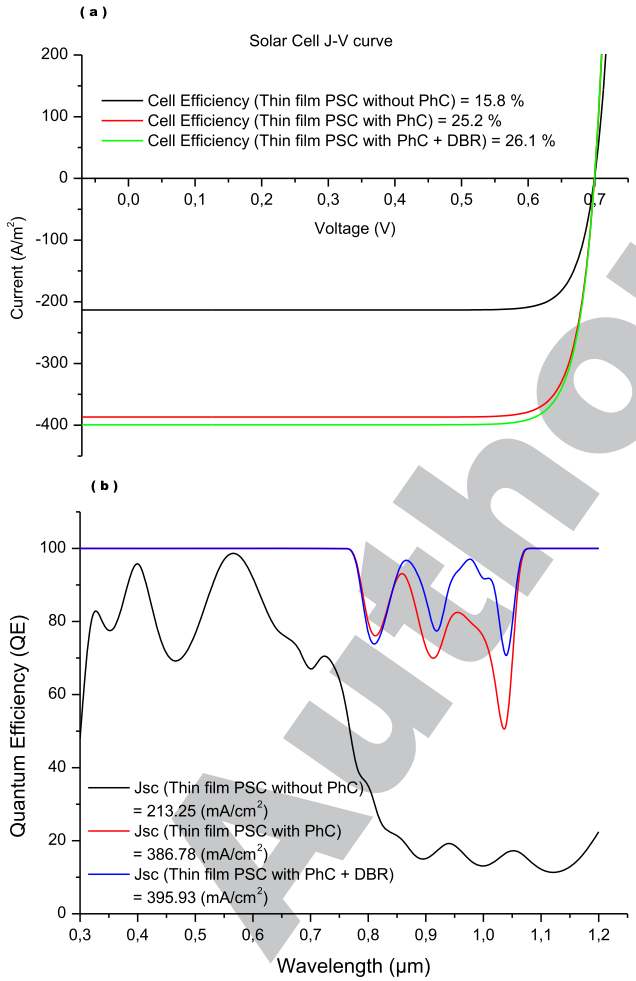

FIG. 7. (a) J–V curve of the proposed thin-film perovskite solar cell without photonic crystal structures (PhCs), with 2D PhCs, and with 2D PhCs + DBR. (b) Quantum Efficiency (QE) vs wavelength for the proposed thin-film perovskite solar cell without PhCs, with 2D PhCs, and with 2D PhCs + DBR.

TABLE III. Comparison of PCE and J_{sc} current for the proposed thin-film perovskite solar cell with and without PhC as a back reflector.

Device structure	PCE (%)	J_{SC} (mA/cm^2)	V_{OC} (V)	FF (%)
Thin film PSC without PhC	15.8	21.3	0.63	58.1
Thin film PSC with 2D PhC	25.2	38.6	1.18	78.49
Thin film PSC with 2D PhC+ DBR	26.1	39.6	1.21	82.85

C. Electrical performance of the proposed nanostructure

Figure 7(a) presents the J–V characteristics of the simulated devices, with the extracted photovoltaic parameters summarized in Table III. It is observed that both the reference structure without 2D photonic crystals (2D PhCs) and the configuration incorporating only the 2D PhCs with a DBR exhibit a relatively lower short-circuit current density (J_{sc}) of 21.3 mA/cm^2 than the other investigated designs. This reduction in photocurrent is consistent with the corresponding external quantum efficiency (EQE) response, as shown in Fig. 7(b), where a noticeable decrease in quantum efficiency is observed across the visible spectrum.

The reduced performance observed in the planar perovskite solar cell (PSC) without photonic crystals (PhCs) can be attributed to lower electron and hole mobilities, which limit charge collection efficiency. In contrast, the structure integrating 2D PhCs alone demonstrates improved an open-circuit voltage (V_{oc}) of 1.18 V, a fill factor (FF) of 78.49%, short-circuit current density (J_{sc}) of 32.14 mA/cm^2, and a resulting power conversion efficiency (PCE) of 25.2%.

The 2D PhCs with a distributed Bragg reflector (DBR) structure exhibit the best performance, achieving an open-circuit voltage (V_{oc}) of 1.21 V, a fill factor (FF) of 82.85%, a short-circuit current density (J_{sc}) of 33.28 mA/cm^2 and a resulting power conversion efficiency

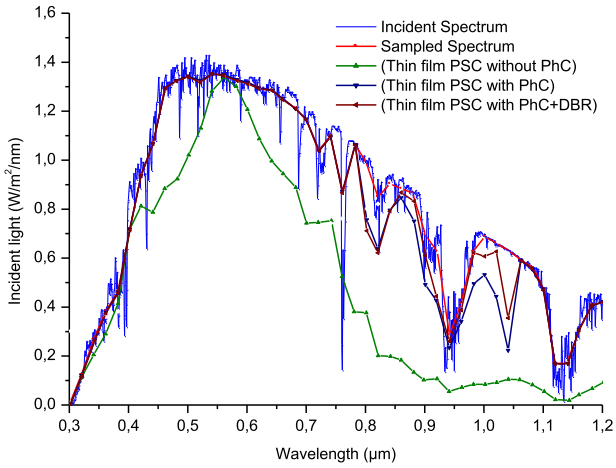

FIG. 8. Simulated absorption spectra of the proposed perovskite solar cell without PhCs, with 2D PhCs, and 2D PhCs +DBR structures illustrating increased absorption across the solar spectrum (0.3–1.2 μm).

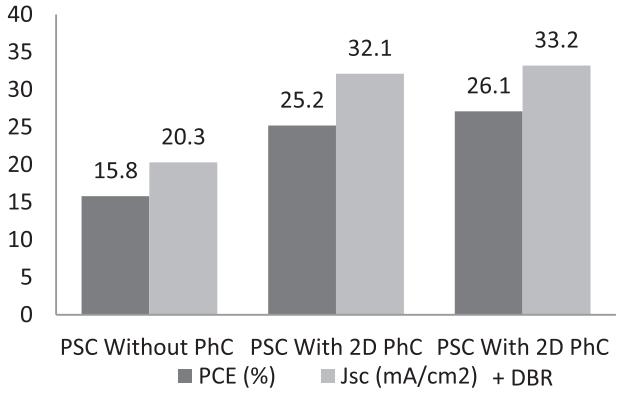

FIG. 9. Comparison of the enhancement in final PCE and short circuit current without PhC, with 2D PhC, and with 2D PhC + DBR.

(PCE) of 26.1%. These enhancements arise from reduced reflection and parasitic optical losses, combined with more effective light trapping, which increases absorption within the perovskite layer.

The graph in Fig. 8 shows the increased absorption of the incident solar spectrum due to photon recycling upon incorporating the PhC as a light trapping structure. The figure also compares the enhancement in final PCE and J_{sc} with and without the PhC.

The final results confirm a substantial enhancement in solar spectrum absorption when PhCs are employed as back reflectors. A direct comparison of devices with and without PhCs (Table III and Fig. 9) shows that both the J_{sc} and overall efficiency nearly double when a PhC is used as a selective wavelength reflector. This clearly highlights the potential of photonic crystal-based designs for boosting the performance of next-generation perovskite solar cells.

V. CONCLUSION

The results demonstrate that incorporating 2D PhCs as light-trapping structures can substantially enhance the PCE of solar cells. Perovskite solar cells, which already hold strong potential to rival silicon-based technologies, further offer the advantages of low-cost fabrication and high efficiency. Organic–inorganic perovskites, such as $CH_3NH_3PbI_3$, can be readily synthesized from lead halide salts and organic amines, and they exhibit favorable properties such as low defect density—owing to their ionic nature—and a high diffusion length-to-absorption length ratio, both of which are critical for achieving large photocurrents. Furthermore, the integration of a tuned DBR enables the design of simple thin-film solar cells suitable for large-scale industrial production. The significant increase in J_{sc} highlights the enhanced generation of photo-induced carriers through photon recycling.

It should be noted, however, that these findings are based on numerical simulations. In practical applications, factors such as contact shading and shunting losses—depending on fabrication methods and environmental conditions—must be taken into account. Given the promising simulated performance, future work will focus on fabricating the proposed structure and assessing its behavior under real-world operating conditions.

AUTHOR DECLARATIONS

Conflict of Interest

The authors have no conflicts to disclose.

Author Contributions

Mounir Bouras: Conceptualization (equal); Data curation (equal); Software (equal); Writing – original draft (equal). **Moufdi Hadjab**: Conceptualization (equal); Data curation (equal); Investigation (equal); Validation (equal); Writing – review & editing (equal). **Maroua Chahmi**: Conceptualization (equal); Formal analysis (equal); Resources (equal); Software (equal). **Salah Khennouf**: Data curation (equal); Methodology (equal); Validation (equal). **Abdelaziz Rabehi**: Conceptualization (equal); Data curation (equal); Investigation (equal); Project administration (equal); Resources (equal); Visualization (equal); Writing – review & editing (equal). **Takele Ferede Agajie**: Formal analysis (equal); Resources (equal); Software (equal); Writing – review & editing (equal). **Abdullah K. Alanazi**: Formal analysis (equal); Funding acquisition (equal); Resources (equal); Software (equal); Validation (equal); Visualization (equal).

DATA AVAILABILITY

The data that support the findings of this study are available from the corresponding author upon reasonable request.

REFERENCES

[1] R. Lin *et al.*, "Monolithic all-perovskite tandem solar cells with 24.8% efficiency exploiting comproportionation to suppress Sn(II) oxidation in precursor ink," Nat. Energy **4**, 864–873 (2019).
[2] A. Kojima *et al.*, "Organometal halide perovskites as visible-light sensitizers for photovoltaic cells," J. Am. Chem. Soc. **131**, 6050–6051 (2009).
[3] G. Yang *et al.*, "Stabilizer-assisted growth of formamdinium-based perovskites for highly efficient and stable planar solar cells with over 22% efficiency," Nano Energy **63**, 103835 (2019).
[4] H. Tao *et al.*, "High absorption perovskite solar cell with optical coupling structure," Opt. Commun. **443**, 262–267 (2019).
[5] B. Chen *et al.*, "Enhanced optical path and electron diffusion length enable high-efficiency perovskite tandems," Nat. Commun. **11**, 1257 (2020).
[6] S. R. Kumavat *et al.*, "Two-dimensional $Ch_3Nh_3PbI_3$ with high efficiency and superior carrier mobility: A theoretical study," J. Phys. Chem. C **123**, 5231–5239 (2019).
[7] S. Albrecht and B. Rech, "Perovskite solar cells: On top of commercial photovoltaics," Nat. Energy **2**, 16196 (2017).
[8] A. Tooghi *et al.*, "High-performance perovskite solar cell using photonic–plasmonic nanostructure," Sci. Rep. **10**, 11248 (2020).
[9] M. H. Mohammadi *et al.*, "NiO@GeSe core-shell nano-rod array as a new hole transfer layer in perovskite solar cells: A numerical study," Sol. Energy **204**, 200–207 (2020).
[10] J. Boroumand *et al.*, "Unified electromagnetic-electronic design of light trapping silicon solar cells," Sci. Rep. **6**, 31013 (2016).
[11] C. Liu *et al.*, "Strategies for growing perovskite films on nanostructured TiO_2 for high performance solar cell," in *IEEE 2nd Electron Devices Technology and Manufacturing Conference (EDTM)* (IEEE, 2018), pp. 107–109.
[12] Z. Li *et al.*, "Facet-dependent, fast response, and broadband photodetector based on highly stable all-inorganic $CsCu_2I_3$ single crystal with 1D electronic structure," Adv. Funct. Mater. **30**, 2002634 (2020).

[13]L. Zheng *et al.*, "Self-powered flexible TiO_2 fibrous photodetectors: Heterojunction with P3HT and boosted responsivity and selectivity by Au nanoparticles," Adv. Funct. Mater. **30**, 2001604 (2020).
[14]K. Chen *et al.*, "Light-trapping schemes for silicon thin-film solar cells via superquadratic subwavelength gratings," Appl. Opt. **58**, 8702–8712 (2019).
[15]S. A. Choudhury *et al.*, "Effect of varying the row and column size of periodic arrays of plasmonic nanoparticles on the energy conversion efficiency of thin-film solar cells," in *International Conference on Electrical, Computer and Communication Engineering (ECCE)* (IEEE, 2017), pp. 44–49.
[16]Z. Yu *et al.*, "Fundamental limit of nanophotonic light trapping in solar cells," Proc. Natl. Acad. Sci. **107**, 17491 (2010).
[17]J. Nelson, *The Physics of Solar Cell* (Imperial College Press, London, United Kingdom, 2008).
[18]I. Borriello *et al.*, "*Ab initio* investigation of hybrid organic-inorganic perovskites based on tin halides," Phys. Rev. B **77**, 235214 (2008).
[19]H. Xiang *et al.*, "Towards highly stable and efficient planar perovskite solar cells: Materials development, defect control and interfacial engineering," Chem. Eng. J. **420**(2), 127599 (2021).
[20]L. P. Lekesi *et al.*, "Developments on perovskite solar cells (PSCs): A critical review," Appl. Sci. **12**, 672 (2022).
[21]G. E. Eperon *et al.*, "Formamidinium lead trihalide: A broadly tunable perovskite for efficient planar heterojunction solar cells," Energy Environ. Sci. **7**, 982 (2014).
[22]J. Hu *et al.*, "Automated design of hybrid halide perovskite monolayers for band gap engineering," npj Comput. Mater. **10**, 140 (2024).
[23]V. Stacchin *et al.*, "Phenothiazine-based self-assembled monolayer with thiophene head groups minimizes buried interface losses in tin perovskite solar cells," Adv. Energy Mater. **15**, 2500841 (2025).
[24]T. Minemoto and M. Murata, "Theoretical analysis on effect of band offsets in perovskite solar cells," Sol. Energy Mater. Sol. Cell. **133**, 8–14 (2015).
[25]S. Das and T. L. Alford, "Improved efficiency of P3HT:PCBM solar cells by incorporation of silver oxide interfacial layer," J. Appl. Phys. **116**, 044905 (2014).
[26]X. Yang *et al.*, "Simultaneously enhancing the efficiency and stability of perovskite solar cells by using P3HT/PEDOT:PSS as a double hole transport layer," Nanomaterials **14**, 1476 (2024).
[27]U. Mandadapu *et al.*, "Design and simulation of high efficiency tin halide perovskite solar cell," Int. J. Renew. Energy Res. **7**(4), 1603–1612 (2017).
[28]H.-J. Du *et al.*, "Device simulation of lead-free $CH_3NH_3SnI_3$ perovskite solar cells with high efficiency," Chin. Phys. B **25**, 108802 (2016).
[29]B. Grote *et al.*, "Quantum-well laser diodes: Temperature and many-body effects," in *Advanced Simulation and Analysis of Optoelectronic Devices*, edited by J. Piprek (■, 2004).
[30]B. Grote *et al.*, "Integration of microscopic gain modeling into a commercial laser simulation environment," Proc. SPIE **4986**, 413–422 (2003).
[31]J. Piprek, *Semiconductor Optoelectronic Devices* (Academic Press, 2003).
[32]D. Nassim *et al.*, "Magneto-photonic crystal micro-cavities in one dimensional photonic crystals fabricated by sol gel process," J. Nanoelectron. Optoelectron. **14**(8), 1189–1193 (2019).
[33]M. Chahmi *et al.*, "Light trapping for absorption control in perovskite-based photovoltaic solar cells," Prog. Electromagn. Res. Lett. **108**, 41–48 (2023).
[34]Y. Raoui *et al.*, "Performance analysis of $MAPbI_3$ based perovskite solar cells employing diverse charge selective contacts: Simulation study," Sol. Energy **193**, 948–955 (2019).
[35]M. Hadjab *et al.*, "A numerical optimization study of CdS and $Mg_{0.125}Zn_{0.875}O$ buffer layers in CIGS-based solar cells using *wx*AMPS-1D package," Int. J. Model. Simul. **42**(2), 179–191 (2022).
[36]S. S. Li, *Semiconductor Physical Electronics*, 2nd ed. (Springer, 2006).
[37]J. Nelson, *The Physics of Solar Cells: Photons In, Electrons out* (Imperial College Press, 2003).
[38]E. D. Palik, *Handbook of Optical Constants of Solids* (Academic Press, San Diego, CA, 1991).
[39]DiffractMod v2015.06 User Guide, Synopsys, Inc., Opt. Solutions Group, New York, 2015.
[40]M. Bouras *et al.*, "Efficient magneto-optical TE/TM mode converter in a hybrid structure made with a SiO_2/ZrO_2 layer coated on an ion-exchanged glass waveguide," Optik **157**, 658–666 (2018).
[41]M. Bouras, "High-performance silicon nitride grating-coupled SPR sensors for gas detection and biosensing," Prog. Electromagn. Res. Lett. **118**, 93–98 (2024).
[42]D. Pudis *et al.*, "PDMS-based nanoimprint lithography for photonics," Commun. Sci. Lett. Univ. Zilina **16**(1), 15–20 (2014).
[43]T. Atouani, M. Mostefaoui, B. Dennai, A. Rabehi, Y. A. Alsabah, and M. Benghanem, "Tension loss analysis at the electrode interface of a dye-sensitized solar cell (DSSC)," AIP Adv. **15**(7), 075307 (2025).
[44]A. M. Younsi, M. Elbar, and A. Rabehi, "Structural, electronic, and optical properties of perovskites $CaATe_3$ (A = Zr or Hf): A theoretical investigation," Semiconductors **58**(12), 984–992 (2024).
[45]R. Daha, M. Bouloudenine, A. Khiat, C. V. Gomez, M. La Pietra, I. E. Tibermacine, S. Alleg *et al.*, "Enhancement of cobalt ferrite properties through rare earth ion doping," Semiconductors **58**(12), 993–1005 (2024).
[46]F. Mekaret, A. Rabehi, B. Zebentout, S. Tizi, A. Douara, S. Bellucci, M. Guermoui *et al.*, "A comparative study of Schottky barrier heights and charge transport mechanisms in 3C, 4H, and 6H silicon carbide polytypes," AIP Adv. **14**(11), 115302 (2024).
[47]O. Baitiche, F. Bendelala, A. Cheknane, A. Rabehi, and E. Comini, "Numerical modeling of hybrid solar/thermal conversion efficiency enhanced by metamaterial light scattering for ultrathin PbS QDs-STPV cell," Crystals **14**(7), 668 (2024).
[48]A. Douara, A. Rabehi, M. Guermoui, R. Daha, and I. E. Tibermacine, "Impact of AlN buffer layer thickness on electronic and electrical characteristics of $In_{0.17}Al_{0.83}N$/GaN high-electron-mobility transistor," Phys. Solid State **66**(6), 157–164 (2024).